Medical Image Analysis (1999) volume 3, number 2, pp 175–185

Alignment of magnetic-resonance brain datasets with the stereotactical coordinate system

Frithjof Kruggel* and D. Yves von Cramon

Max-Planck-Institute of Cognitive Neuroscience, Stephanstraße 1b, 04103 Leipzig, Germany

Abstract
Neuroanatomical and neurofunctional studies are often referenced to high-resolution magnetic-resonance brain datasets. For the analysis of the cortical surface, mapping of functional information on to the cortex or visualization, it is necessary to remove the outer surfaces of the brain. For intersubject comparison, it is useful to align the dataset with a coordinate system and introduce a spatial normalization. We describe an image processing chain that combines all of these steps in an interaction-free procedure. We report on a period of 2 years of routine application of this procedure, with >250 successfully processed datasets from healthy subjects and patients with various forms of brain damage.

Keywords: brain atlas, brain peeling, MRI, stereotactical coordinate system

Received July 10, 1998; revised November 10, 1998; accepted November 27, 1998

1. INTRODUCTION

The structural variability of the individual human brain has led to different attempts to define a common reference system. While the most common approach was developed by Talairach 40 years ago (Talairach and Tournoux, 1988), the high spatial resolution of recent neuroimaging techniques calls for more precise methods of comparing individual brains. Most notably this has fostered the 'Human Brain Project', a joint project to develop a computerized multimodal brain atlas (Mazziotta *et al.*, 1995). Common to these approaches is the registration within a coordinate system and a method for the spatial normalization of the individual brain dataset. The 'stereotactical coordinate system' has found the most widespread acceptance. It uses the anterior (AC) and posterior commissure (PC) as reference structures. Their midpoint defines the origin of a right-handed coordinate system. There is little agreement, however, as to what method of spatial normalization will best serve the demands of the problem. First-order normalization as suggested by Talairach (the so-called Talairach space) has found widespread use (Collins *et al.*, 1994; Friston *et al.*, 1995). However, due to their limited accuracy, they might be replaced in the near future by second-order methods such as elastic or viscous transformations (Thompson and Toga, 1996) or symbolic atlases (Kruggel, 1995).

Besides neurosurgery, the introduction of a reference system helps to assign functional activity (as revealed by fMRI, EEG, MEG and PET) to anatomical locations. For the visualization of cortical functional activation registered with a high-resolution anatomical dataset, it is first necessary to segment the individual brain from its outer layers (i.e. skin, facial muscles, skull, meninges). This operation is often referred to as 'brain shelling' or 'brain peeling'. To ease intersubject comparisons, it is useful to align brain scans with a common reference system.

In this article, we describe how a sequence of image processing steps and a few neuroanatomical heuristics work together to allow the identification of AC and PC automatically. This procedure can easily be combined with the removal of the non-brain parts in the dataset, which otherwise requires tedious manual work. As an example of spatial normalization, we will also introduce a mapping into the Talairach space.

We would like to review relevant definitions and anatomical details in the next section. Section 3 explains details of the algorithms used in the procedure. Our method was tested with >250 high-resolution magnetic-resonance (MR)

*Corresponding author
(e-mail: kruggel@cns.mpg.de)

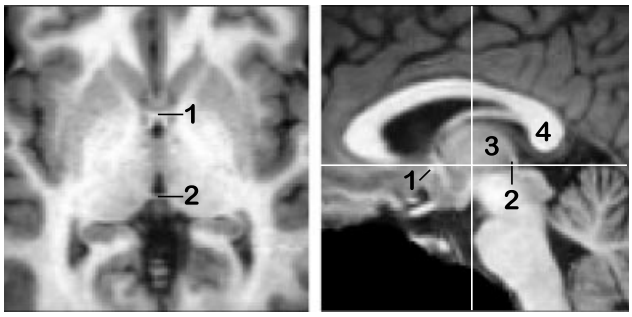

Figure 1. Enlarged slice of an MR dataset in the axial (left) and sagittal (right) direction. Axes of the stereotactical coordinate system are drawn. The numbers correspond to: (1) anterior commissure; (2) posterior commissure; (3) adhaesio interthalamica and (4) splenium of the corpus callosum.

brain datasets acquired with different scanners using different imaging sequences. In Section 4, we report our results. The concluding discussion weights advantages, problems and possible pitfalls of this procedure.

2. DEFINITION OF THE STEREOTACTICAL COORDINATE SYSTEM

In 1957, Talairach and Tournoux (1988) introduced a reference system for the human brain. Its primary concern was to aid neuroradiologists and neurosurgeons in locating specific structures in the core brain, the basal ganglia, from landmarks accessible by the then available imaging techniques (X-ray and pneumencephalography). They selected the AC and PC as reference structures to define the orientation of the coordinate system. These commissures are small fibre bundles that connect both hemispheres and thus cross the mid-sagittal plane of the brain (see Figure 1). Both delimit the third ventricle on its anterior and posterior margin. A recipe for the manual procedure of defining the stereotactical coordinate system is given by

- locate AC and PC in the mid-sagittal plane of the brain,
- draw a line touching the superior edge of the AC and the inferior edge of the PC (Figure 1),
- define the positive x-direction along the AC–PC line in the sagittal direction (front-to-back), and
- define the positive z-direction to lie perpendicular to x in the mid-sagittal plane (axial direction, top-to-bottom), thus
- the positive y-direction is perpendicular to the mid-sagittal plane (coronal direction, left-to-right).

A spatial normalization is introduced by the definition of a proportional grid in a bounding box around the cerebrum. This box is given by

- the highest point of the parietal cortex,
- the most posterior point of the occipital cortex,
- the lowest point of the temporal cortex,
- the most anterior point of the frontal cortex, and
- the most lateral point of the parieto-temporal cortex.

Note that the cerebellum is only partially included in the box. This box is divided:

- in the x-direction into nine parts, of which four are equally spaced before AC, one is defined by the distance AC–PC and the remaining four lie behind PC,
- in the y-direction into eight equally spaced parts,
- in the z-direction into 12 parts, of which eight are equally spaced above AC–PC and the remaining four lie below AC–PC.

Note that this definition yields a piecewise linear mapping in each half-space. A location in the brain is referenced with respect to a 'box' in this grid. A brain dataset may be mapped by a piecewise linear transformation into the Talairach space. This method of spatial normalization gained widespread acceptance in neurosurgery and neuroradiology. Talairach did not define a metric and a directional order in this space. Thus, Fox *et al.* (1985) suggested shifting the origin of the coordinate system to AC, and defined a right-handed coordinate system as follows:

- the x-direction runs from the leftmost point of the brain (-64 mm) to rightmost point ($+64$ mm),
- the y-direction extends from the back (-104 mm) to the front ($+68$ mm),
- the z-direction defines the topmost point as $+72$ mm.

This definition corresponds to a linear mapping. The brain mapping community accepted this definition for the positional description of focal brain activity centres as revealed by PET, fMRI, EEG and MEG. Thus, we will denote this definition as the Talairach–Fox space (Fox *et al.*, 1995; Friston *et al.*, 1995).

More recent approaches to spatial normalization followed this definition, but replaced the method for spatial normalization by higher-order procedures (Christensen *et al.*, 1996; Thompson and Toga, 1996). Although AC and PC are visually detectable in high-resolution MR images, the alignment with this coordinate system is still a manual procedure to be performed by an expert. We would like to show that this procedure may be automatized and easily integrated within a brain peeling procedure.

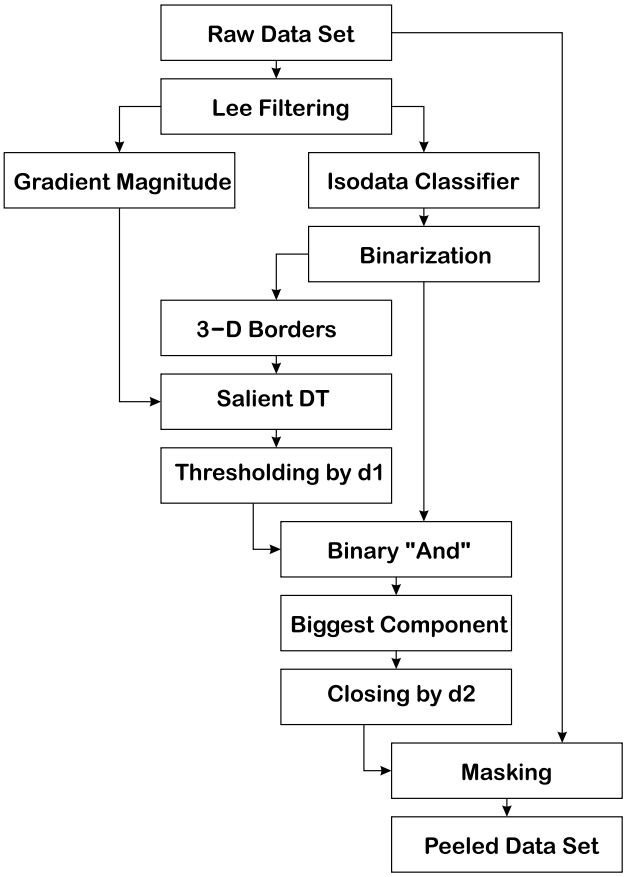

Figure 2. Schematic overview of the data flow in the peeling procedure. For example results of the intermediate steps, see Figure 3.

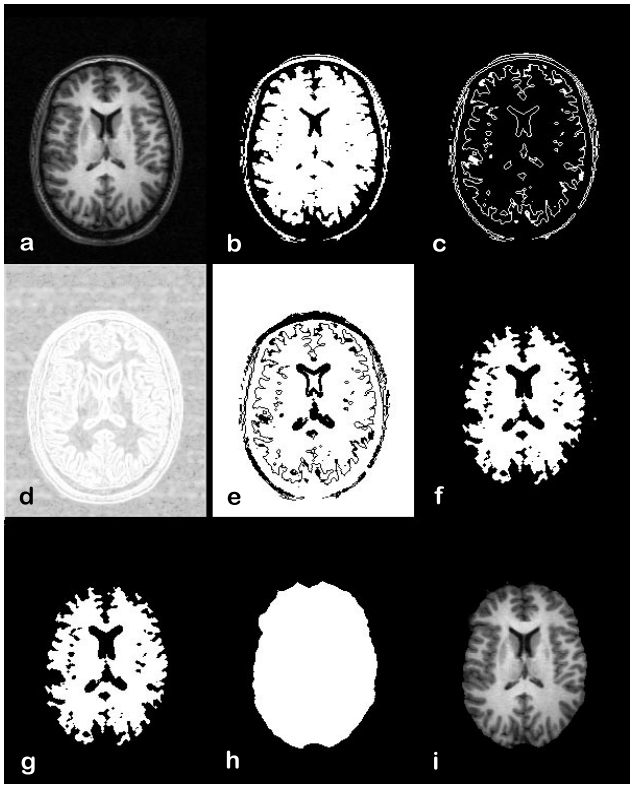

Figure 3. Schematic overview of intermediate results of the peeling procedure.

3. DETAILS OF THE PROCEDURE

For studying the individual brain anatomy as well as comparisons between brain structures of different subjects, it is advantageous to have a high-resolution MR dataset, in which the non-brain parts are removed and which is aligned to a standard coordinate system. Such a dataset is stored in a 'brain database' and is available for further anatomical or functional studies. For the adoption, we need to (i) find and apply a binary mask to extract the brain, (ii) determine and apply an affine transform to align the brain with the coordinate system and (iii) apply any method of spatial normalization. We cover only the analysis of single-echo T_1-weighted images, which commonly serve as a base for neuroanatomical analysis and can be achieved within 5–15 min.

Most of the steps in this processing chain involve standard algorithms, so we simply refer to the literature for the algorithmic background. Only key processing steps and anatomical heuristics are discussed in more detail.

3.1. Brain peeling

The first part of the processing chain removes the outer layers of the brain in the MR scan of a head. We will refer to this procedure as 'brain peeling'. The sequence of articles published so far underline the importance of this procedure (Cline *et al.*, 1990; Brummer *et al.*, 1993; Joliot and Mazoyer, 1993; Ardekani *et al.*, 1994; Arata *et al.*, 1995; Kapur *et al.*, 1995; Kruggel and Lohmann, 1997; Atkins and Mackiewich, 1998). The key point in any peeling procedure is the approach of separating the brain from its layers. A starting point for our work is given by Brummer *et al.* (1993) who proposes the use of a distance transform. However, all algorithms in our processing chain operate fully in three dimensions. For a data flow scheme of the sequence see Figure 2, intermediate results are shown in Figure 3.

The dataset is preprocessed with an edge-preserving noise filter (Lee, 1983; Figure 3a). A fast unsupervised clustering algorithm (Isodata, see e.g. Lohmann, 1998) segments the

d_3	d_2	d_3
d_2	d_1	d_2
d_3	d_2	d_3

d_2	d_1	d_2
d_1	0	0
0	0	0

0	0	0
0	0	0
0	0	0

Figure 4. Forward mask m used to compute a distance transform. Distances are $d_1 = 0.9016$, $d_2 = 1.289$ and $d_3 = 1.615$. The backward mask is symmetric about the centre of this mask.

image into two classes (Figure 3b). Voxels belonging to the tissue class are collected and the set of border voxels is formed (Figure 3c). A distance transform (Figure 3d) of this border image is computed (Beckers and Smeulders, 1992; Borgefors, 1996) and thresholded to include only voxels which are spaced at least a distance d_1 from the border (Figure 3e). We perform a binary 'and' operation of this mask with the set of tissue voxels (Figure 3f) and select the largest connected component (Figure 3g). This object is enlarged by a distance d_2 using a morphological closing operator to form our brain mask (Figure 3h). This mask is used to extract brain voxels from our (unfiltered) input dataset (Figure 3i).

Instead of using a simple Euclidean distance transform (DT) we used a salient variant, which is gradient-weighted. Rosin and West (1995) describe various approaches for computing a salient DT, one of which is based on the modification of a standard DT algorithm [for a more detailed description, see Borgefors (1996)]:

1. The three-dimensional (3-D) voxel dataset containing the tissue voxels is input. Distances d at tissue voxels are set to 0, at non-tissue voxels to an arbitrary large value. In addition a gradient magnitude image g of the noise-filtered input dataset is computed.

2. At each pixel at location (x, y, z) in the image, a local distance mask m (see Figure 4) is centred. Each non-zero mask value $m_{a,b,c}$ in the local 26-neighbourhood is added to the value of the corresponding voxel d in the distance map, weighted by the local gradient magnitude g:

$$s_{a,b,c} = \frac{d^i_{x+a,y+b,z+c} + m_{a,b,c}}{g^i_{x+a,y+b,z+c}}. \qquad (1)$$

3. The set of indices (a, b, c) at the most salient measure s (i.e. the minimum value) is selected.

4. Using these indices, the distance $d_{x,y,z}$ at the central voxel is updated:

$$d^{i+1}_{x,y,z} = d^i_{x+a,y+b,z+c} + m_{a,b,c}. \qquad (2)$$

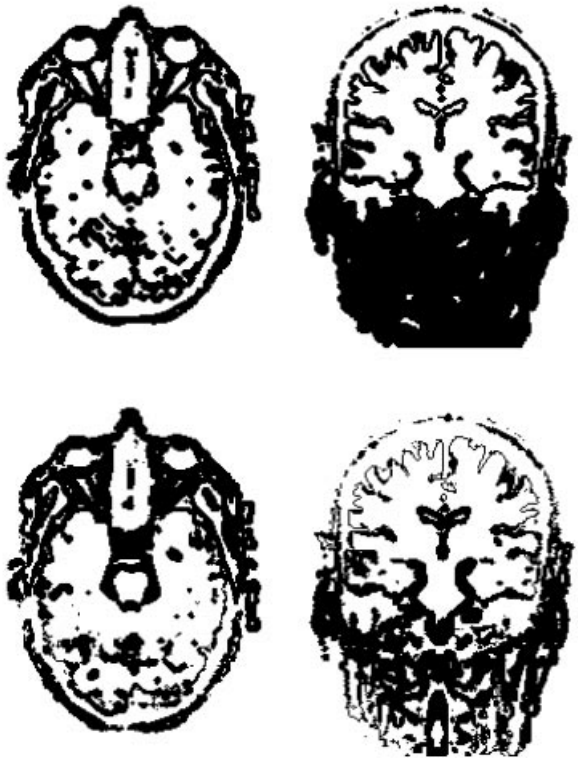

Figure 5. Mask used to separate the brain from its outer layers, computed using a standard DT (top row) and the salient variant (bottom row). The salient variant allows reduction the peeling distance d_1 and achieves a better segmentation of the cortex.

5. Repeat steps 2–4 for all voxels in a forward and a backward pass.

This weighting by the edge magnitude results in a faster rise of distance values along sharp edges, respectively a slower rise in regions of low gradients. For an example of the results of a standard DT versus the salient variant, see Figure 5.

This processing chain necessitates only two parameters, d_1 and d_2. The first distance specifies the separation between the brain and the outer layers. Typical values range between 1.0–3.0 mm with a standard setting of 1.6 mm. The distance d_2 is used to enlarge the first mask and is usually left at 4.0 mm.

3.2. Introduction of the coordinate system

To detect the AC/PC bundles and to register the dataset with the coordinate system, we need to perform the following steps: (i) determine the mid-sagittal plane; (ii) detect the commissures; (iii) find the crossing between the plane and both commissures; (iv) compute the centre and the axes; and

(v) compute an affine transform for the peeled image and apply it.

3.2.1. Finding the mid-sagittal plane

The mid-sagittal plane is defined as a plane separating both brain hemispheres. It is often mistakenly identified as the interhemispheric cleft or the brain symmetry plane. In most individuals, the left hemisphere is slightly larger (especially the occipital lobe), so the interhemispheric cleft is bent to the right-hand side. For this reason, the assumption of a symmetry plane is just a first-order approximation. For the detection of AC and PC, we are interested in a small area of this plane in the core brain and may thus introduce only a small error by assuming planarity.

A plane S in $\mathcal{R}^3$ is given by a plane normal n and a distance d from the origin to that plane. We define a scalar domain Ω in $\mathcal{R}^3$, which is discretized as a 3-D finite-element grid v. The scalar quantity $I(v_i)$ at a voxel v_i is 1 on tissue and 0 on background voxels. One could think of two options for approximating the mid-sagittal plane:

- detect the interhemispheric cleft by minimization of tissue voxels in a plane:

$$S = \arg\min \left\{ \sum_{v_i \in S(d,n)} I(v_i) | (d,n) \in \mathcal{R} \times \mathcal{R}^3 \right\} \quad (3)$$

- determine a symmetry plane between tissue voxels in both hemispheres:

$$S = \arg\min \left\{ \sum_{I(v_i)=1} |d + n \cdot v_i| \, | (d,n) \in \mathcal{R} \times \mathcal{R}^3 \right\}. \quad (4)$$

With both approaches we found that the desired plane does not lie in the global minimum of the parameter space [for a comparable discussion, see Ardekani *et al.* (1997)]. The first approach will find a plane outside the brain (no tissue voxels), the second may converge to any plane for which tissue voxels on both sides are balanced. So we had to restrict the search space by introducing constraints. An initial estimate for the mid-sagittal plane S is determined most easily by segmenting the centre of both eyes (e_1, e_2) and defining a symmetry plane $\hat{S} = (\hat{d}, \hat{n})$ between them using

$$\hat{n} = \frac{e_1 - e_2}{|e_1 - e_2|} \quad \text{and} \quad \hat{d} = \hat{n} \cdot \frac{e_1 + e_2}{2}. \quad (5)$$

For the detection of the vitreous body of the eyes, we started from the tissue voxels acquired in the brain peeling step (see Figure 3b). A morphological opening separated small bridges between the eyes and the skin. We labelled connected components and computed their shape descriptions (centre, size and moments). From these shape descriptions, we selected spherical components of 4000–7000 voxels. If more than two components were found, we selected the two most similar which were 50–75 mm apart.

We implemented different optimization schemes for both weighting functions Equations (3) and (4), among them Newton's method, the conjugate gradient method, Powell's method, and genetic optimization. This Newtonian scheme was found to be most stable:

```
optimizePlane(image v, float d, normal n)
{
shift = shift_max; angle1 = angle2 = angle_max;
while (shift > shift_min && angle1 > angle_min && ..) {
   // shift plane in the direction of the normal
   // by +shift and evaluate the cost function Eqn. (4)
   w1 = computeSymmetry(v, d+shift, n);
   // shift plane in the direction of the normal
   // by -shift and evaluate the cost function Eqn. (4)
   w2 = computeSymmetry(v, d-shift, n);
   // compute the shift where w would be 0
   shift = 2 * w1 * shift / (w2-w1);
   // apply that shift and narrow interval
   d = d + shift;
   shift = shift / 2;
   // a similar procedure is applied for angle1
   // and angle2 to optimize the plane normal
   ...
   }
return d, n;
}
```

Starting from the initial guesses $S(\hat{d}, \hat{n})$, we apply modifications to the plane parameters by shifting it closer or further away from the origin (variable *shift*) and by tilting it in both axes of the plane (*angle1*, *angle2*). The cost function *computeSymmetry*() returns a measure according to Equation (4), which is minimized while allowing modifications in successively smaller intervals. We found starting values for *angle_max* of 10° and *shift_max* of 10 mm to be sufficient. In non-pathological datasets, we found the angle between the initial plane normal $\hat{n}$ and its optimized value to be $<2.5°$, and the difference of the distance $\hat{d}$ to be <5 mm. This algorithm converges within five to ten iterations and needs $\sim$30 s computation time on a standard workstation.

3.2.2. Detection of AC and PC

The next and crucial step in the adoption of the stereotactical coordinate system is the detection of the two reference structures. Commissures are fibre bundles which connect both hemispheres and thus may be regarded as 'shape bottlenecks' between them. If we span a constant gradient field between both hemispheres, these bottlenecks are detectable in the steady state as regions of high flow (Mangin *et al.*, 1996). Thus, AC and PC are detectable as local flow peaks in the mid-sagittal plane.

Given a domain Ω in $\mathcal{R}^3$, we can formulate for any regular potential $u(x, y, z)$ the well-known law of conservative flow:

$$\frac{\delta u}{\delta t} = -\nabla u \quad \text{on } \Omega. \tag{6}$$

We set a Dirichlet condition on the boundary $\Gamma = \delta\Omega$ as $u = g$ on Ω. Equation (6) is discretized by introducing a finite-element grid v in Ω, which corresponds to the binarized peeled brain. The boundary Γ is given by a set of voxels on two planes which are parallel to the mid-sagittal plane, in the left and the right hemisphere. We introduce the diffusion constant d and a boundary potential g, and use a well-known iterative integration scheme (Gerig *et al.*, 1992) to solve Equation (6) using the six-neighbourhood N_6^*:

$$U(v_i, t) = g \quad \text{on } \Gamma \tag{7}$$

$$U(v_i, t+1) = U(v_i, t) + \tfrac{1}{6} d \sum_{v_j \in N_6^* \cap \Omega} U(v_j, t) - U(v_i, t). \tag{8}$$

This finite-differencing scheme is known to converge very slowly. We improved the convergence speed by introducing a multi-resolution grid. The system is computed first on a model downsampled by 2^m, then the solution is distributed to the next higher resolution and refined. For a single time step at a specific resolution we formulated the algorithm as:

```
computePotentialFlow(image v)
{
// initialize potential on the boundary gamma (7)
setBorderPotential(v);
// compute flow for a time step in the 3-D voxel array v
for (all vi in v) {
   // do not operate on background voxels
   if (I(vi) == 0) continue;
   // compute flow from voxels in the 6-neighborhood (8)
   flow = 0; n = 0;
   for (all vj in the 6-neighborhood of vi) {
      if (I(vj) == 0) continue;
      flow = flow + U(vj) - U(vi);
      n++;
   }
   // update flow at this voxel
   U(vi) = U(vi) + flow / n;
}
}
```

At each time step, a set of border voxels in the right and the left hemisphere is initialized with a constant high (respectively low) potential. On the whole 3-D dataset, we used four resolution steps with 100, 200, 600 and 1000 time steps (from lowest to highest resolution). We finally assumed a steady state and computed the flow rate ΔU through a voxel v_i in its six-neighbourhood N_6 by

$$\Delta U(v_i) = \sum_{v_j \in N_6^* \cap \Omega} [U(v_j) - U(v_i)] / U(v_i). \tag{9}$$

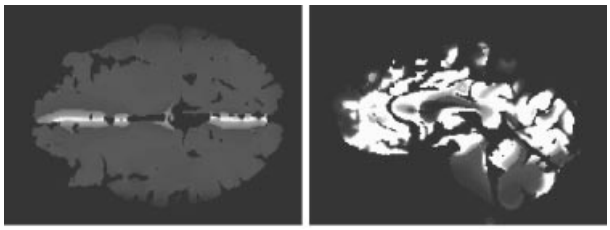

Figure 6. Flow-rate image computed from a binarized peeled dataset. Bright areas correspond to regions of high flow. Shown are an axial slice (left) in the AC–PC plane and the mid-sagittal plane (right). By comparison with Figure 1, one can easily detect AC and PC as flow maxima in this image.

This flow rate clearly depicts shape bottlenecks in the 3-D dataset, as shown in Figure 6. Because we are interested in flow maxima only, the choice of the diffusion constant and the border potential are arbitrary.

Among other structures connecting both hemispheres, we found AC and PC as peak flow regions. For a complete dataset this algorithm needs ~40 min of computation time. To detect AC and PC only, we can limit the search space to a small subvolume. We tested several heuristics to define this subvolume. The centre of mass (cm) in a peeled brain was surprisingly stable in the area between the splenium of the corpus callosum (see structure 4 in Figure 1), the habenula and the adhaesio interthalamica (see structure 3 in Figure 1). On a vector between the centre of the eyes $ce = (e_1 + e_2)/2$ and the centre of mass cm, an initial estimate $\widehat{ac}$ for the position of AC is given by

$$\widehat{ac} = ce + 0.7(cm - ce). \tag{10}$$

Likewise, an estimate $\widehat{pc}$ for the PC position is found at

$$\widehat{pc} = cm - 0.1(cm - ce)_z \tag{11}$$

where $(cm - ce)_z$ denotes the cranio-caudal component of this difference vector. These heuristics were found to be valid in all of our datasets with a deviation <3 mm. One can now limit the search space for AC and PC to a small subvolume of $50 \times 50 \times 30$ voxels computed from cm and ce, so that the computation time of the flow algorithm reduces to 40 s. We cut this flow-rate image with the mid-sagittal plane and search for flow maxima using $\widehat{ac}$ and $\widehat{pc}$ as starting points. From these flow maxima, we adjusted the coordinates to find the superior edge of the AC and the inferior edge of the PC.

Now we were able to introduce the Talairach–Fox space: with AC as the centre, we denoted the line passing through AC and PC as the y-axis of the coordinate system, defined the x-axis from the plane normal n, and the z-axis as perpendicular to both x and y. We computed an affine transform

to map the peeled brain image into this reference system which includes rescaling in 3-D to an isotropic resolution. We finally yielded a peeled brain dataset with isotropical resolution and registered to a standardized coordinate system. One should note that the steps to detect AC and PC are parameter-free and do not need any user interaction.

3.2.3. Normalization in the Talairach space

As outlined in Section 2, the Talairach space is defined by the extremal points of the brain in each direction of space. These points are easily determined from a binarized peeled image. We store the extremal points as attributes in the image dataset and compute a Talairach mapping when necessary. Three-dimensional renderings of an example dataset are shown in Figure 7.

4. IMPLEMENTATION AND RESULTS

The image processing sequence outlined above was implemented as separate modules of the BRIAN visual editor (Kruggel and Lohmann, 1996). Once the procedure had stabilized and the range of the parameters d_1 and d_2 had been determined, the processing chain was repackaged into a single module. Further results were achieved by this stand-alone module. Although this processing chain consists of a number of separate steps, careful reuse of intermediate results limited the total processing time to ∼12 min on a conventional workstation. Time-consuming steps were found with the initial Lee filter and the computation of the gradient image for the salient distance transform. Both steps are easily parallelized, reducing the computation time to 3 min using eight processors.

The robustness of this processing chain was tested with 80 high-resolution MR brain datasets, acquired on eight different MR scanners (Siemens Impact at 1.0 T, Siemens Vision at 1.5 T, Phillips Gyroscan at 1.5 T, GE Signa at 1.5 T, and Bruker at 3.0 T) at five different locations (see the Acknowledgements). We used T_1-weighted 3-D sequences, including 3-D GRE FLASH (24), SE FLASH (4), and MDEFT (49). For three datasets, sequence information was not available. Each dataset contained 128 sagittal (or axial) slices with an in-plane resolution between 0.86 and 1.0 mm and a plane-to-plane distance of between 1.4 and 1.5 mm. All datasets were checked visually by an expert (neuroradiologist) to exclude gross artefacts (motion, folding), developmental abnormalities or the presence of lesions. Processing consisted of (i) conversion from the machine-specific format (DICOM or MEDSPEC) into the Vista format (Pope and Lowe, 1994), (ii) extraction of the spatial resolution information (field-of-view and interslice distance) and patient orientation information from the machine format, (iii) application of this image processing chain and (iv) visual inspection of the results.

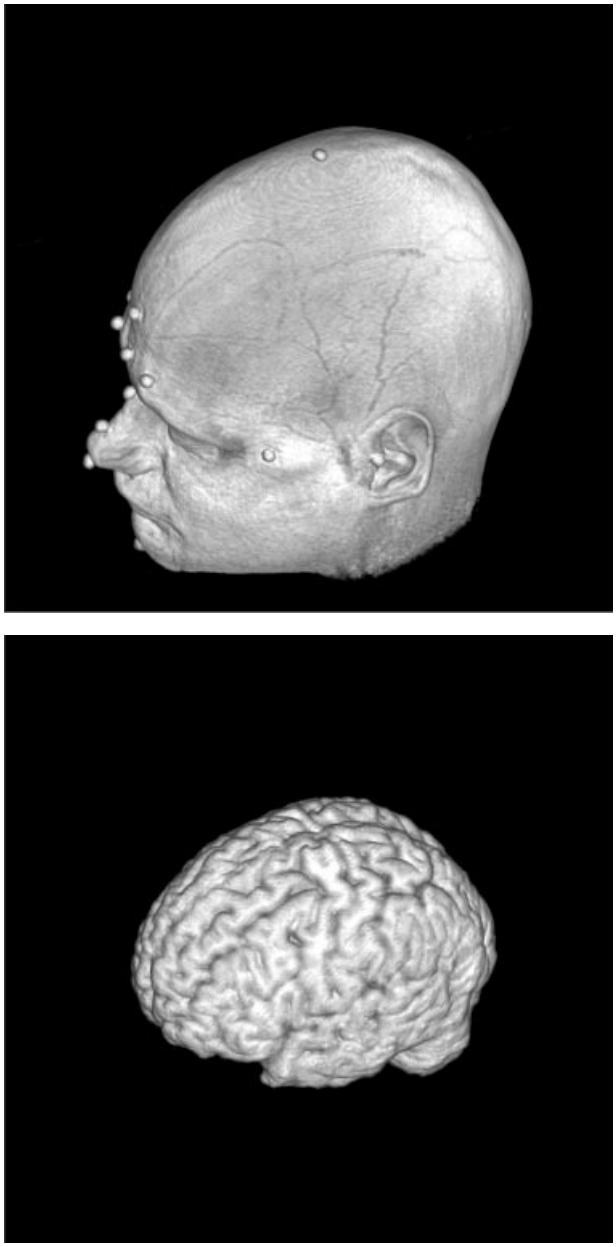

Figure 7. Three-dimensional rendering of a sample head MR dataset and the output of this procedure, a peeled brain. Beads were placed on the forehead for registration purposes.

The only user-adjustable parameters of our procedure are the peeling distances d_1 and d_2 (Subsection 3.1), of which in practice only a variation of d_1 in a range of 1.0–3.0 mm is

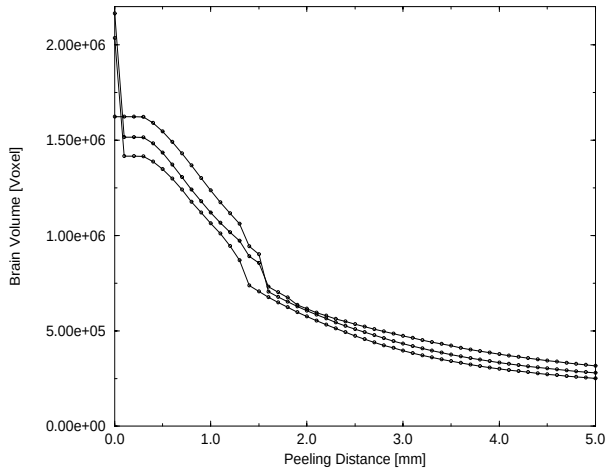

Figure 8. Brain volume after peeling as a function of the peeling distance d_1 in three cases. The default distance of 1.6 mm is found at the knee of this sigmoid curve.

useful. We will now report experiences with our procedure in this evaluation set of brain scans.

In 58 of 80 cases (73%), our processing chain succeeded on the first run with standard settings. In the remaining 22 cases, the peeling was inaccurate with parts of the outer layers still being attached to the brain. Raising the distance d_1 from the default value to 2.0–2.4 mm resolved this problem in another 19 cases (23%). A sufficient peeling was not achievable in three cases (4%) only, where the left mediobasal temporal cortex was attached to the meninges. A solution may be provided by introducing a morphological opening with a small kernel between steps e and f in the peeling procedure. However, this may have adverse effects on other brain regions. Thus careful inspection is necessary to guarantee a proper peeling.

In general, the peeling distance d_1 should be chosen to be as low as possible. Typically, the volume of the peeled brain follows a sigmoid curve which is dependent on d_1 (see Figure 8). The optimum value of d_1 is found at the lower knee of this curve. We experimented with adaptive procedures that vary the peeling distance and determine the optimum by examining the remaining volume, where $\sim$10 cycles between peeling steps e to g are necessary. In practice however, we favour using the standard setting and check the result over the additional computation time.

Using a gradient-weighted DT, we achieved a distinct separation in high-contrast regions (i.e. at the neocortical convexity of the brain), and a broader separation zone in low-contrast regions (i.e. the base of the brain). However, this gradient-weighted DT introduced a dependence of the peeling distance d_1 from the image contrast. An optimum range has to be determined for a particular imaging protocol. The values are given for our high-contrast MDEFT datasets. For a typical GRE protocol, where the T_1 contrast is generally lower, we applied distances between 2.0–3.2 mm.

In this evaluation set of 80 scans, we never found it necessary to modify the peeling distance d_2 from its default value of 4 mm. In $>$250 scans we needed to raise this distance to higher values (say, 6 mm) in only cases where high values of d_1 were applied. In datasets of children, we had to lower d_2 to 3 mm.

In 96% of the cases, the reference structures AC and PC could be detected and a coordinate system adapted. Careful assessment of the three negative cases revealed the detection of eye clusters as a problematic step. By visual inspection of the datasets, no clear border between the vitreous body of the eye and the surrounding air could be made, with the consequence that none or only one eye was detected. Asking subjects to keep their eyes closed during scanning removed this problem.

To assess the quality of the procedure, we compared the position of the origin and the orientation of the axes with reference alignments, which were generated manually. The deviation between the manually and automatically determined origin was 1.2 ± 0.4 mm (range 0–2.5 mm). The maximal rotational deviation before alignment were 4° around x, 10° around y and 8° around z. After alignment, the deviation between the manually and automatically rotated axes were $0.8 \pm 0.5^\circ$ (range 0–1.5°).

Although our procedure was designed to work with T_1-weighted datasets, the peeling part was applied with proton-density (PD)- weighted head scans as well. However, AC and PC are not detectable in this weighting, so the alignment does not work. The procedure is not applicable to T_2-weighted datasets or sets of a few (say, $<$60) T_1-weighted slices. In datasets with comparatively high between-plane distances, the connectivity of structures (i.e. the scalp) in 3-D might not be traceable.

The application of this procedure to pathological datasets adds another dimension of complexity. To underline advantages and limits of this procedure we will now discuss cases with typical intracranial pathological findings. In Figure 9, we collected brain data sets with (i) a subcortical infarction in the deep territory of the left middle cerebral artery, (ii) a subtotal infarction of the right middle cerebral artery, (iii) an occlusive hydrocephalus and (iv) an astrocytoma of the left temporal lobe.

Focal small (hypointense or hyperintense) lesions, as in case (i), do not pose any problems to this algorithm. Even mass lesions [case (ii)] are treated well by this

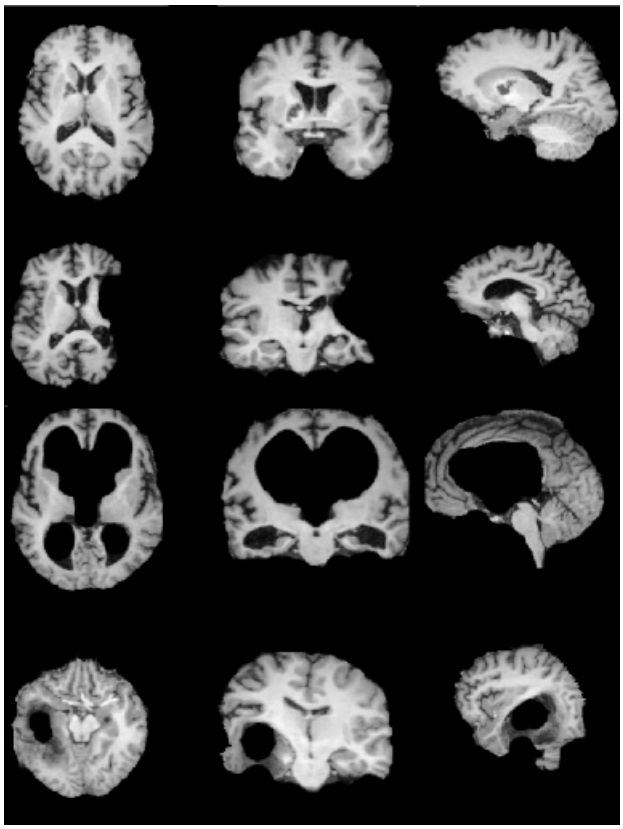

Figure 9. Peeling results of four pathological cases. Case (i) (first row): small infarction in the left globus pallidus and interior capsule; case (ii) (second row): subtotal infarction of the right middle cerebral artery; case (iii) (third row): occlusive hydrocephalus; case (iv) (fourth row): astrocytoma of the left temporal lobe.

procedure. In this case however, the symmetry assumptions made for the determination of the mid-sagittal plane are grossly violated. We therefore used the automatic peeling part only and supplied AC and PC directly. Note also that this extensive lesion led to a shrinking of the brain in the cranio-caudal direction [see the coronal slice of Figure 9(ii)]. Similarly, we found no major limitation in datasets of brain atrophies, i.e. in patients with Alzheimer's disease. A 3-D reconstruction of these datasets reveals the huge extent of this right-sided lesion: $\approx\frac{2}{3}$ of the right hemisphere was damaged by the infarct (see Figure 10). If symmetry is maintained, the automated procedure works well [case (iii)].

However, there are cases where most of the heuristics incorporated in our procedure are rendered invalid by pathological findings. In case (iv), due to a midline shift to the

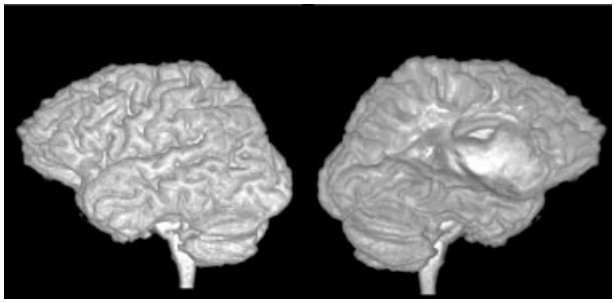

Figure 10. Three-dimensional rendering of case (iv) from Figure 9. A massive tissue loss in the right hemisphere is attributable to a subtotal infarct of the middle cerebral artery.

right side, symmetry assumptions are violated, and we had to specify AC and PC manually. In addition, this patient underwent a partial removal of the skull over a space occupied by this inoperable tumour. In this area, skin and galea followed the brain surface very closely, so that a proper peeling could not be achieved and manual intervention was necessary. Small hyperintense structures in this hypointense lesion may be lost during the peeling if they are unconnected and further away than the peeling distance d_2 from other signal-intensive brain regions (i.e. in the centre of the lesion). When using the partly peeled dataset from this procedure and manually removing the remaining parts of the outer hulls, we achieved a successfully processed dataset in $<$20 min.

Our experience with $\approx$60 MR datasets of pathological cases shows that this procedure works in $>$70% of the cases without any intervention. In cases like that of Figure 9(iii) or (iv) however, a careful check of the results is advisable.

5. DISCUSSION

We described an interaction-free procedure to remove the outer layers of the brain in MR head scans and to adapt the stereotactical coordinate system. By adjusting only one parameter, we were able to segment 96% of T_1-weighted high-resolution datasets acquired on eight different scanners. With the experience of $>$250 successfully processed datasets, we regard this procedure as sufficiently stable for routine use.

A few issues may play an important role in other environments and need to be discussed. The simple but fast unsupervised classification scheme (see Figure 3b) is sensitive to contrast fluctuations due to inhomogeneities in the gradient field of the scanner. A few approaches for inhomogeneity correction in MR datasets were proposed

(Yan and Karp, 1995; Wells *et al.*, 1996; Rajapakse *et al.*, 1998; Sled and Zijdenbos, 1998) and might replace the simple clustering scheme. However, these methods require a considerably higher amount of computation time. With a typical variation of the white matter intensity of $<15\%$ in our datasets, we do not consider inhomogeneities as a real problem. When selecting an imaging protocol for anatomical scanning, one should always favour a high-T_1 contrast over a good signal-to-noise ratio. In particular, the detection of AC and PC are subject to the good definition of the white matter compartment and may fail in datasets with a low-T_1 contrast.

With 60 cases of intracranial pathologies studied so far we certainly cannot claim complete coverage of all types of pathologies. Obviously, heuristics applied in this algorithm must be met in order to yield satisfactory results: (i) both eyes have to be detectable; (ii) in a first approximation, hemispheres should be symmetric; and (iii) no midline shifts be present (due to edema, tumours). MR examination statistics show that these requirements are met in 98% of the normal cases and in $>90\%$ of our cases examined under clinical conditions.

A few other approaches for the registration of brains with the stereotactical coordinate system were proposed. Minoshima (Minoshima *et al.*, 1992; Minoshima, 1993) designed a two-stage registration process that starts by identifying the interhemispheric cleft and then uses empirical rules to automatically locate four points along the AC–PC line. However, because this procedure was designed for PET experiments, these rules are dependent on the tracer distribution applied (Brummer, 1991). Collins *et al.* (1994) used a multiscale cross-correlation for the registration of a sample dataset with an averaged MR brain volume that has been aligned with the Talairach space. A similar approach was described later by Friston *et al.* (1995) and is implemented in the SPM software. They did not detect the reference structures directly and were thus dependent on a successful registration with their model. Recently, a second approach to detect the reference structures of the stereotactical coordinate system was described by Verard *et al.* (1997). Similar to our procedure, they first detected the mid-sagittal plane and then used a complex scene analysis to define the position of AC and PC. They reported a precision in a range comparable to our figures, and a high robustness.

This procedure was integrated into our preprocessing routine for head scans of test subjects as well as patients. Results are placed in a common brain database that serves as a further reference for anatomical and functional evaluations. We consider this sequence as a basic step to study focal or diffuse brain diseases and for monitoring their changes with time. We have just begun to touch the use of image processing in monitoring disease processes.

ACKNOWLEDGEMENTS

We would like to thank the following people for the generous supply of datasets: A. Horsch (Technical University, München), J. Rajapakse (NIH, Bethesda), B. Maeß (Forschungszentrum Jülich), H. Steinmetz (University Clinic Düsseldorf and D. Norris (MPI-CNS, Leipzig). As a courtesy to the community, this procedure is available on request.

REFERENCES

Arata, L. K., Dhawan, A. P., Broderick, J. P., Gaskil-Shipley, M. F., Levy, A. V. and Volkow, N. D. (1995) Three-dimensional anatomical model-based segmentation of MR brain images through principal axes registration. *IEEE Trans. Biomed. Eng.*, 42, 1069–1078.

Ardekani, B. A., Braun, M., Hutton, B. F. and Kanno, I. (1994) Automatic detection of arachnoid contours in MR images. In *Visualization in Biomedical Computing, VBC'94, Proc. SPIE* Vol. 2359, pp. 402–410. SPIE, Washington, DC.

Ardekani, B. A., Kershaw, J., Braun, M. and Kanno, I. (1997) Automatic detection of the mid-sagittal plane in 3D brain images. *IEEE Trans. Med. Imag.*, 16, 947–952.

Atkins, M. S. and Mackiewich, B. T. (1996) Fully automatic segmentation of the brain in MRI. *IEEE Trans. Med. Imag.*, 17, 98–107.

Beckers, A. L. D. and Smeulders, A. W. M. (1992) Optimization of length measurements for isotropic distance transformations in three dimensions. *Image Understanding*, 55, 296–306.

Borgefors, G. (1996) On digital distance transforms in three dimensions. *Comp. Graphics Image Processing*, 64, 368–376.

Brummer, M. E. (1991) Hough transform detection of the longitudinal fissure in tomographic head images. *IEEE Trans. Med. Imag.*, 10, 74–81.

Brummer, M. E., Mersereau, R. M., Eisner, R. L. and Lewine R. R. J. (1993) Automatic detection of brain contours in MRI datasets. *IEEE Trans. Med. Imag.*, 12, 153–166.

Christensen, G. E., Miller, M. I. and Vannier, M. W. (1996) Individualizing neuroanatomical atlases using a massively parallel computer. *IEEE Computer*, 18, 32–36.

Cline, H. E., Lorensen, W. E., Kikinis, R. and Jolesz, F. (1990) Three-dimensional segmentation of MR images of the head using probability and connectivity. *J. Comput. Assis. Tomogr.*, 14, 1037–1045.

Collins, D. L., Neelin, P., Peters, T. M. and Evans, A. C. (1994) Automatic 3D intersubject registration of MR volumetric data in standardized Talairach space. *J. Comput. Assis. Tomogr.*, 18, 192–205.

Fox, P. T., Perlmutter, J. S. and Raichle, M. E. (1985) A stereotactic method of anatomical localization for positron emission tomography. *J. Comput. Assis. Tomogr.*, 9, 141–153.

Fox, P. T., Mikiten, S., Davis, G. and Lancaster, J. (1995) Brain map: a database of human functional brain mapping. In *Functional Neuroimaging: Technical Foundations*, pp. 95–105. Academic Press, Orlando, FL.

Friston, K., Ashburner, J., Frith, C., Poline, J. B., Heather, J. and Frackowiak, R. (1995) Spatial registration and normalization of images. *Human Brain Mapping*, 2, 165–189.

Gerig, G., Kübler, O., Kikinis, R. and Jolesz, F. A. (1992) Nonlinear anisotropic filtering of MRI data. *IEEE Trans. Med. Imag.*, 11, 221–232.

Joliot, M. and Mazoyer, B. M. (1993) Three-dimensional segmentation and interpolation of magnetic resonance brain images. *IEEE Trans. Med. Imag.*, 12, 269–277.

Kapur, T., Grimson, W. E. L. and Kikinis, R. (1995) Segmentation of brain tissue from MR images. In *Computer Vision, Virtual Reality and Robotics in Medicine, Lecture Notes in Computer Science*, Vol. 905, pp. 429–433. Springer-Verlag, Heidelberg.

Kruggel, F. (1995) Automatical adoption of anatomical masks to the neocortex. In *Computer Vision, Virtual Reality and Robotics in Medicine, Lecture Notes in Computer Science*, Vol. 905, pp. 231–236. Springer-Verlag, Heidelberg.

Kruggel, F. and Lohmann, G. (1996) BRIAN (brain image analysis)—a toolkit for the analysis of multimodal brain datasets. In *Computer Assisted Radiology, CAR'96*, pp. 323–328. Elsevier, Amsterdam.

Kruggel, F. and Lohmann, G. (1997) Automatical adoption of the stereotactical coordinate system in brain MRI datasets. In *Information Processing in Medical Imaging, IPMI'95, Lecture Notes in Computer Science*, Vol. 1230, pp. 471–476. Springer-Verlag, Heidelberg.

Lee, J. S. (1983) Digital image smoothing and the sigma filter. *Comp. Graphics Image Processing*, 24, 255–259.

Lohmann, G. (1998) *Volumetric Image Analysis*. Wiley and Teubner, Chichester.

Mangin, J. F., Regis, J. and Frouin, V. (1996) Shape bottlenecks and conservative flow systems. In *Mathematical Methods in Biomedical Image Analysis*, pp. 319–328. IEEE Press, Washington, DC.

Mazziotta, J. C., Toga, A. W., Evans, A., Fox, P. and Lancaster, J. (1995) A probabilistic atlas of the human brain: theory and rationale for its development. *Neuroimage*, 2, 89–101.

Minoshima, S. (1993) Automated detection of the intercommisural (AC–PC) line for stereotactic localization of functional brain images. *J. Nucl. Med.*, 34, 322–329.

Minoshima, S., Berger, K. L., Lee, K. S. and Mintun, M. A. (1992) An automated method for rotation correction and centering of three-dimensional functional brain images. *J. Nucl. Med.*, 33, 1579–1585.

Pope, A. R. and Lowe, D. G. (1994) Vista: a software environment for computer vision research. In *Computer Vision and Pattern Recognition, CVPR'94*, pp. 768–772. IEEE Press, Washington, DC.

Rajapakse, J. C., Kruggel, F. and von Cramon, D. Y. (1998) Segmentation of MR images with intensity inhomogeneities. *Image Vision Comput.*, 16, 165–180.

Rosin, P. L. and West G. A. F. (1991) Salient distance transforms. *Graphical Models and Image Processing*, 57, 483–521.

Sled, J. G. and Zijdenbos A. P. (1998) A nonparametric method for automatic correction of intensity nonuniformity in MRI data. *IEEE Trans. Med. Imag.*, 17, 87–97.

Talairach, J. and Tournoux, P. (1988) *Co-planar Stereotactic Atlas of the Human Brain*. Thieme, Stuttgart.

Thompson, P. and Toga, A. W. (1996) A surface-based technique for warping three-dimensional images of the brain. *IEEE Trans. Med. Imag.*, 15, 402–471.

Verard, L., Allain, P., Travere, J. M., Baron, J. C. and Bloyet, D. (1997) Fully automatic indentification of AC and PC landmarks on brain MRI using scene analysis. *IEEE Trans. Med. Imag.*, 16, 610–616.

Wells, W. M., Grimson, W. E. L., Kikinis, R. and Jolesz, F. A. (1996) Adaptive segmentation of MRI data. *IEEE Trans. Med. Imag.*, 15, 429–442.

Yan, M. X. H. and Karp, J. S. (1995) An adaptive Bayesian approach to three-dimensional MR brain segmentation. In *Information Processing in Medical Imaging, IPMI'95*, pp. 201–213. Kluwer Academic Publishers, Amsterdam.